Numerical simulations of shallow groundwater flow and heat transport in a continuous permafrost setting under the impact of climate warming

Masoumeh Shojae Ghias*, René Therrien, John Molson & Jean-Michel Lemieux
Department of Geology & Geological Engineering, Université Laval, Québec, Québec, Canada
Centre d'études Nordiques, Université Laval, Québec, Québec, Canada

*Corresponding author: masoumeh.shojae-ghias.1@ulaval.ca

For re-submission to: Canadian Geotechnical Journal
June 2018

Abstract

Numerical simulations of coupled groundwater flow and heat transport are used to address how hydrogeological conditions can affect permafrost dynamics. The simulations are based on a 2D vertical-plane conceptual model of a study site at the Iqaluit Airport, Nunavut, Canada, which includes a 50 m deep permafrost terrain with a shallow active layer, overlain by a paved taxiway with winter snow-covered embankments. Coupled groundwater flow and advective-conductive heat transport with freeze-thaw dynamics, temperature-dependent porewater freezing functions and latent heat are included in the model. The simulation results show that a smooth (low-slope) freezing function with a higher residual unfrozen moisture content produced a deeper thaw front compared to that using a steeper freezing function, generating a maximum increase in the depth to permafrost of 17.5 m after 268 years. Permafrost thaw rates in high-permeability zones within a heterogeneous system were also relatively higher compared to an otherwise equivalent homogeneous soil, resulting in a maximum increase of 2.6 m in the depth to permafrost after 238 years. As recharge water cools while flowing along the upgradient permafrost table, advectively-

driven heat transport is paradoxically shown to temporarily increase the height of the permafrost table in downgradient areas.

Keywords: Permafrost, Groundwater, Numerical modelling, Heterogeneity, Freezing function

1 Introduction

Permafrost terrain, which covers about 24% of the land surface in the Northern Hemisphere (Zhang et al. 2003), are among the most sensitive environments to climate change, especially in cold regions where climate warming is expected to increase dramatically. Recent climate warming throughout the Arctic has resulted in extensive permafrost degradation (Serreze et al. 2000) , which in turn affects hydrogeological processes, alters ecosystem functionality, increases carbon dioxide and methane fluxes from the ground, and reduces infrastructure stability (McKenzie and Voss 2013; Kurylyk et al. 2014). Other hydrogeological and environmental factors can also contribute to accelerate permafrost degradation and change the subsurface thermal regime in these sensitive areas. For example, the presence of snow cover in combination with climate warming has been shown to exacerbate permafrost degradation (Zhang et al. 2008; Fortier et al. 2011; Shojae Ghias et al. 2016) since it generally acts as an insulating buffer layer that reduces heat losses from the ground during winter, thus keeping the ground warmer during the cold months.

As a result of climate warming, serious environmental impacts and new engineering challenges are expected in these vulnerable regions. A comprehensive understanding of the hydrogeological processes that control permafrost dynamics in response to increasing air temperatures is essential to develop effective mitigation measures against these impacts.

Permafrost degradation is linked to changes in climate and to subsurface heat transport, which is governed by thermal conduction and by thermal advection in areas of groundwater flow. The interactions among climate warming, permafrost and groundwater flow have been recently investigated with coupled groundwater flow and heat transport models by, among others, Rowland (2011), Ge et al. (2011), Bense et al. (2012), Wellman et al. (2013), McKenzie and Voss (2013), Shojae Ghias et al. (2015 and 2016), and Kurylyk et al. (2014a). Kane et al. (2001) showed that advective heat transport can be significant in permafrost settings, while simulations by Ling and Zhang (2003) suggested that neglecting advective heat transport can decrease the reliability of predictions of the ground thermal regime. McKenzie and Voss (2013) simulated coupled groundwater flow and heat transport, including complex heterogeneity within a regional-scale permafrost setting, using the USGS Sutra-Ice model. Their simulations demonstrated that the influence of advective heat transport depends strongly on the hydraulic gradients as well as on the heterogeneity and anisotropy of the subsurface hydraulic conductivity. They also showed that the time required for complete thaw of a permafrost zone by conduction only could be reduced by one-third if advection is also accounted for. Although geological heterogeneities can have a controlling effect on groundwater flow in permafrost terrain (McKenzie and Voss 2013), the influence of heterogeneity on permafrost thaw has not been investigated in most past studies. Numerical simulations by Bense et al. (2012) included heterogeneity in soil permeability due to ice formation, but did not account for intrinsic soil heterogeneity. They concluded that groundwater flow is strongly connected to the initial distribution of permafrost and on the changes in permeability as the permafrost thaws.

The temperature-dependent unfrozen moisture content can strongly affect the soil permeability, thermal conductivity and heat capacity. Spatial variations in the unfrozen moisture content can also affect advective heat transport. Although the freezing function depends strongly

on the soil type (as shown in the experimental work of Watanabe 2011), it is usually assumed to be uniform despite natural soil heterogeneity. McKenzie et al. (2007) examined the sensitivity of an advancing freezing front to the freezing function and associated release of latent heat by simulating the Neumann problem (Carslaw et al. 1959). They found that the shape of the freezing function plays a very important role in controlling the rate and extent of ice formation. A greater amount of latent heat released over a smaller temperature range (i.e. with a steep freezing function) can thus delay migration of the freezing front. Using the Lunardini (1985) solution with advective heat transport, Kurylyk et al. (2014b) concluded that neglecting latent heat during pore-ice thaw can over-predict the depth of the thawing front.

Although ongoing research focuses on the impact of climate change on permafrost, there are still many knowledge gaps in the understanding of the subsurface thermal regime in response to climate warming. As concluded by Kurylyk et al. (2014), a comprehensive understanding of permafrost behaviour due to climate variations will demand additional studies that include advective heat transport as well as model calibration against observed field measurements, and will require integrating climate warming models with coupled flow and heat transport models.

The principal objective of this study is to help fill this knowledge gap by addressing the influence of hydrogeological controls on permafrost degradation in the context of climate change. We expand upon the work presented by Shojae Ghias et al. (2016) by completing a sensitivity analysis using additional hydrogeological simulation scenarios based partly on the field-calibrated 2D vertical model across Taxiway Alpha at the Iqaluit Airport, Nunavut, Canada. Coupled groundwater flow and heat transport scenarios are simulated for 268 years under future climate scenario projections proposed by the Intergovernmental Panel on Climate Change (IPCC 2007). Simulations are designed to investigate the effect of subsurface heterogeneity, and the form of the freezing function on the subsurface thermal regime.

2 Methods

In this section, the numerical model used for the simulations is first presented, followed by a description of the study site and the conceptual model, as well as an overview of the simulations reported here.

2.1 Numerical model

The HEATFLOW/SMOKER model (Molson and Frind 2017) was used for all simulations presented here. The model simulates coupled density-dependent groundwater flow and heat transport with freezing and thawing, latent heat and the associated temperature-dependent parameters of density, viscosity, thermal conductivity, heat capacity, unfrozen water content, and relative permeability. The model has been tested against various freeze-thaw benchmark problems including analytical solutions proposed by Lunardini (1985) and numerical benchmarks from the INTERFROST consortium (Grenier et al. 2018; Rühaak et al. 2015).

The flow equation as solved in the HEATFLOW/SMOKER model is written as:

$$\frac{\partial}{\partial x_i}\left[K_{i,j}(T)\left(\frac{\partial \psi}{\partial x_j}\right) + \rho_r(T)\,\overline{n}_j \right] = S_S \frac{\partial \psi}{\partial t} \qquad (1)$$

where x_i are the 3D spatial coordinates (m), $K_{i,j}\ (T)$ is the temperature-dependent hydraulic conductivity tensor (m s^{-1}), ψ is the equivalent freshwater head (m), $\rho_r(T)$ is the temperature-dependent relative density of water (kg m^{-3}), $\overline{n}_j$ is a unit vector in the vertical (z) direction (-), S_s is the specific storage (m^{-1}), and t is time (s).

HEATFLOW/SMOKER couples the flow equation with the general advective-dispersive heat transport equation defined as:

$$-\frac{\partial}{\partial x_i}\left(\theta S_w c_w \rho_w v_i T\right)+\frac{\partial}{\partial x_i}\left(\overline{\lambda}+\theta S_w c_w \rho_w D_{ij}\right)\frac{\partial T}{\partial x_j}+Q=\frac{\partial\left(C_o T\right)}{\partial t} \quad (2)$$

where θ is the porosity (-), S_w is the unfrozen water saturation (-), c_w is the specific heat of water (J kg^{-1} °C^{-1}), ρ_w is the density of water (kg m^{-3}), v_i is the groundwater velocity (m s^{-1}), T is temperature (°C), $\overline{\lambda}$ is the bulk thermal conductivity of the porous medium (J m^{-1} s^{-1} °C^{-1}), D_{ij} is the hydrodynamic dispersion coefficient (m^2 s^{-1}), Q is a thermal source/sink term (J m^{-3} s^{-1}), C_o is the heat capacity (J m^{-3} °C^{-1}), x_{ij} are the spatial dimensions (m) and t is time (s). For the sake of simplicity, we assume here that hydrodynamic thermal dispersion is negligible compared to thermal diffusion (thus, it is assumed that $D_{ij} = 0$).

The bulk thermal conductivity is defined as a function of the volumetric water, ice and solid fractions and is defined by:

$$\overline{\lambda} = \theta S_w \lambda_w + \theta S_i \lambda_i + (1-\theta)\lambda_s \quad (3)$$

where subscripts w, i and s represent the water, ice and solid phases, respectively, with S being the phase saturation and λ the phase thermal conductivity. In Equation (2), the heat capacity of the porous medium C_o is given by:

$$C_o = \theta S_w c_w \rho_w + \theta S_i c_i \rho_i + (1-\theta) c_s \rho_s + \theta \rho_i L\left(\frac{\partial S_w}{\partial T}\right) \quad (4)$$

where L is the latent heat of water (3.34×10^5 J kg^{-1}).

In freeze-thaw systems, the (unfrozen) water saturation S_w in the above equations is replaced by the temperature-dependent fraction of unfrozen moisture (or saturation of unfrozen water), defined by the function W_u:

$$W_u(T) = (1-p)\cdot e^{(-(T/q)^2)} + p \tag{5}$$

where p is the terminal (residual) fraction of unfrozen moisture at a very low (negative) temperature and q is an empirical parameter affecting the curvature of the W_u function. As q increases, the W_u function becomes smoother (with a lower slope) and thus the unfrozen water saturation decreases more slowly with decreasing temperature. Note that this function is not meant to reproduce freezing point depression due to saline water or solute exclusion, which is neglected here.

Temperature variations also affect the permeability of a porous medium as ice forms or melts within the pore space. As permafrost thaws, for example, the unfrozen water saturation increases, which increases the relative permeability (k_r). In this study, the relative permeability function defined by Jame (1980) is used, modified with a minimum relative permeability constrained to 10^{-6}, defined as:

$$k_r(T) = \max\left[10^{-\Omega\cdot\theta(1-Wu(T))}, 10^{-6}\right] \tag{6}$$

where Ω is an empirically-derived impedance factor. Temperature-dependent fluid density and viscosity are defined in Molson and Frind (2017) and the model assumes local (grain-fluid) thermal equilibrium.

The thermal flux J_i (J m^{-2} s^{-1}) across a conceptual heat-exchange boundary layer located at the top surface boundary is expressed as:

$$J_i = \gamma \cdot (T_a - T_s) + (q.c_w \rho_w).(T_q - T_s) + B_{zf} \quad (7)$$

where γ is a heat exchange coefficient (J m^{-2} s^{-1} °C^{-1}) (Palmer et al. 1992), T_a is the given transient air temperature (°C), T_s is the ground surface temperature (°C) (computed by the model), T_q is the temperature of the recharge water, and B_{zf} (J m^{-2} s^{-1}) is an independent heat flux. The numerical model allows T_a, T_q and γ to vary in time due to seasonal changes. The heat transfer coefficient γ is computed as the ratio of the surface-layer thermal conductivity to its thickness, and was considered here as a single calibration parameter.

2.2 Model set-up

The conceptual model in this study is inspired by the site model developed by Shojae Ghias et al. (2016) to represent the climate, hydrogeological and surface conditions at the Iqaluit Airport, Nunavut, Canada. The airport is located in the south-eastern part of Baffin Island, (63º45' N, 68º33' W) (Figure 1a,b), and lies within a continuous permafrost zone. The referenced two-dimensional cross-sectional model, shown in Figure 2, is 100 m long and 50 m deep and is oriented transversely to Taxiway Alpha, which connects the airport runway to the apron. The conceptual model used by Shojae Ghias et al. (2016) contained several geological units, representative of the subsurface geology at the site. However, the intent here is to present the study as a general sensitivity analysis on a simplified conceptual model and to provide insight into general thermal behaviour, rather than providing definitive predictions at this particular field

site. In this context, for simplicity and to highlight the effect of key parameters, the subsurface geology is represented here by a single geological unit (Unit 1) assuming properties representative of a sandy material. All model parameters are presented in Tables 1 and 2.

A 3D finite element mesh (using rectangular prism elements) was generated to discretize the domain for a unit-width vertical cross-section. A uniform horizontal nodal spacing of 1 m was used, while the vertical spacing varies from 0.5 m (from 0 to 49 m elevation) to 0.1 m (from 49 to 50 m elevation). The final mesh contains 22,018 nodes and 10,800 elements.

Boundary conditions for flow and heat transport are shown in Figure 2. The top boundary is assumed to represent a sloping water table, and is assigned hydraulic head values that decrease from the left to the right allowing groundwater recharge into the domain. The watertable gradient is assumed to be 0.001 and a maximum hydraulic head of 49 m is assigned to the top left corner. The left boundary corresponds to a bedrock contact which is assumed impermeable while the bottom boundary within the bedrock is also assumed impermeable. Depending on the transient frozen/thawed state of the active layer, groundwater can exit the domain under natural gradient conditions through fixed heads equal to 48.9 m assigned along the right boundary.

For heat transport, the left and right boundaries are assigned a zero temperature gradient, thus assuming that advective heat flux dominates over lateral conductive heat transport. At the bottom boundary, a heat flux of 0.03 W m^{-2} is assigned, assuming a bulk thermal conductivity of 3.0 J m^{-1} s^{-1} °C^{-1} and a geothermal gradient of 0.01 °C m^{-1} (from Leblanc et al. 2015). The top boundary is assigned a Cauchy condition that combines conductive and advective heat fluxes. The conductive heat flux at the top boundary represents heat exchange across a conceptual heat transfer layer located at the interface between the atmosphere and the subsurface. This heat exchange is driven by a temperature gradient across the surface layer that depends on the difference between the (known) air and (simulated) ground temperatures (Equation 7). The

advective heat flux at the top boundary originates from groundwater recharge. The heat transfer coefficient of the exchange layer (γ in Equation 7) and the additional heat flux (B_{zf}) were determined during calibration, as described below. Advective heat transfer is also allowed during the summer from infiltrating rainwater, which was assumed to be at the prevailing air temperature.

2.3 Overview of simulations

The simulations designed for the sensitivity analysis are listed in Table 3. Cases 1 and 2, representing a steep and a smooth freezing function, respectively, are designed to assess the effect of the freezing function for conduction only (Case 1a, 2a) and advection-conduction (Case 2a, 2b). These two cases assume that the subsurface is homogeneous, with properties similar to that of a sandy soil, and with a uniform porosity. Finally, Case 3 assumes that the subsurface is heterogeneous with a spatially-variable hydraulic conductivity and porosity distribution, for conduction only (Case 3a) and advection-conduction (Case 3b).

The initial reference time (t=0) for all flow and heat transport simulations is the year 2012, at which time the maximum depth of the active layer is about 1.6 m at the sides of the domain and 1.2 m at the center. Initial temperatures for year 2012 were generated numerically with the model by applying observed air temperatures over a spin-up period during 1971-2012 (including seasonal variations), until the system reached quasi- (year-to-year) thermal equilibrium. The initial temperature for the spin-up period starting in 1971 was assumed uniform throughout the domain at -5 °C, which is the current mean annual ground temperature observed at Iqaluit.

All simulations were run for 268 years, until 2280, by which time the model predicts that all permafrost will have completely disappeared. Climate projections for the simulations were obtained from Global Circulation Model (GCM) outputs from IPCC (2007) for a 90-year period

(2011-2100) that were downscaled using the delta change method (Roosmalen et al. 2007). The maximum projected temperature increases are 1.46 °C, 3.02 °C, and 5.22 °C for the CGM-derived time periods 2011-2040, 2041-2070 and 2071-2100, respectively. As also applied by McKenzie and Voss (2013), the HEATFLOW-SMOKER simulations assume that the rate of temperature increase beyond 2100 follows the rate generated by the GCM for the period 2011-2100 (Figure 3).

Convergence criteria for all simulations were 0.01 m for hydraulic heads and 0.05 ˚C for temperatures. The maximum time step for the flow and heat transport solutions was set to 1 day to ensure convergence and numerical stability.

The heat transfer coefficient and the surface heat flux were calibrated through back-calculated ground surface temperatures derived by employing the "n-factor" approach of Lunardini (1978). These n-factors are defined as the ratios of freezing indices and thawing indices between the ground surface and air temperature. Ratios were calculated for both winter snow-covered ground (taxiway shoulders) and snow-free ground (central taxiway) and were assumed independent of climate change.

Initially, mean ratios (n-factors) between observed ground and air temperatures at Iqaluit were extracted from field data collected from 2010-2014 by Leblanc et al. (2015). These ratios were then applied to the air temperatures employed in the present numerical model to obtain corresponding ground surface temperatures. The average freezing and thawing ratios were 0.6 and 1.4, respectively, on each side of the winter snow-covered taxiway, and 0.8 and 1.5 respectively, at the center of the domain (taxiway) which is free of winter snow.

The heat transfer coefficient (γ) and the temperature-independent heat flux (B_{zf}) were then calibrated against these estimated ground temperatures. The final calibrated heat transfer coefficient across the taxiway shoulders varies over each year between 4 J m^{-2} s^{-1} $°C^{-1}$ (during

winter when insulated by snow) and 30 J m^{-2} s^{-1} °C^{-1} (during summer). Since the taxiway is snow-free all year, its γ-value remained constant at 30 J m^{-2} s^{-1} °C^{-1}.

Over the taxiway shoulders covered with winter snow, and along the snow-free taxiway itself, the temperature-independent heat flux (B_{zf}) also varies each year, from a minimum of 10 J m^{-2} s^{-1} (during the winter), increasing to 230 J m^{-2} s^{-1} (during the summer). This flux accounts for additional surface heat exchange processes including thermal radiation.

Some simplifying assumptions have been made in the model. First, a single type of freezing function was assigned for the heterogeneous system (Cases 3a, 3b), whereas a mixed function would be expected depending on the grain size distribution. Climate-dependent temporal changes in the recharge rate were also not directly considered, although recharge in the model was allowed to change seasonally and yearly across the fixed-slope watertable depending on the underlying temperature-dependent permeability. In addition, although the unsaturated zone is accounted for in the heat transport system, only a fully-saturated model was assumed for the flow system. Finally, freezing point depression due to solute exclusion is neglected (to simplify the system and since solute concentrations are normally low for such shallow systems), and although a seasonal snow cover is included on the taxiway embankments (as part of the surface heat-transfer layer), variations in snow depth expected from a warming climate are not considered. Snowmelt was not considered in the model and is assumed to occur rapidly, with much of it running offsite, and thus would not significantly impact the thermal regime of subsurface. Although the importance of snow cover on permafrost degradation is highlighted in this study, variations in the type of snow, including changes in density, moisture content and porosity, are not considered here.

In this paper "the depth to permafrost" or "frost depth" represents the distance from ground surface to the top of the permafrost (or permafrost table), which includes a shallow active layer that undergoes seasonal freeze-thaw.

3 Results

3.1 Effect of the freezing function ($W_u(T)$)

The effect of the freezing function on the thermal permafrost regime for conductive as well as advective-conductive heat transport is evaluated in Case 1 and Case 2 (Table 3). Each of the comparisons (Cases 1a,b-2a,b) applies a different freezing function for one type of soil representative of sand (Figure 4). The freezing function parameters that appear in Eq. 5, namely the terminal unfrozen water saturation at very low temperature (p) and the shape factor (q), are assigned values of 0.1 and 1.0, respectively, for Cases 1a,b (steep freezing function), while p = 0.2 and q = 3.0 for Cases 2a,b (smooth freezing function) (Table 2). These parameters were selected based on existing reference data representing experimental freezing function curves (Watanabe et al. 2011), which show more gradual variations in the unfrozen water during phase transition and a higher residual unfrozen water saturation for a finer soil compared to a coarser soil. Uniform soil properties are considered for Cases 1a,b and 2a,b, as shown in Table 1, with the only difference being the different freezing functions.

For the sake of simplicity and to allow isolating the effect of the freezing function alone, a constant and homogeneous intrinsic (unfrozen state) hydraulic conductivity was assumed in Cases 1 and 2. Nevertheless, the effective hydraulic conductivity still varies depending on the type of soil since the relative permeability (Equation 6 and Table 2) depends on the unfrozen

water content function $W_u(T)$ (Equation 5), which is assumed to be different between the finer soil (smooth freezing function) and coarser soil (steep freezing function). The same reasoning applies for assuming a constant intrinsic thermal conductivity for Cases 1 and 2, while in each case the thermal conductivity will still depend on the temperature-dependent unfrozen water content (Equation 3).

3.1.1 Seasonal variations of the subsurface thermal regimes

The simulated temperature distributions after 88 years for conduction only, assuming a steep freezing function (Case 1a) and smooth freezing function (Case 2a), are depicted in Figure 5 for the months of March, May and September. In each case, the soil zone bounded by arrows identifies where water and ice co-exist between the soil particles and thus where the system is undergoing phase change. Between these temperature limits, the unfrozen water saturation varies as a function of temperature, depending on the freezing function. Based on the parameters assigned herein for the freezing function (Table 2 and Figure 4), the phase transition zone is located between 0 °C and -2 °C for Case 1 and between 0 and about -6 °C for Case 2.

For each selected month at 88 years, temperatures for Case 1a (Figure 5a) are almost everywhere warmer than for Case 2a (Figure 5b). The phase transition zone in the case assigned with a steep freezing function is thus less extensive vertically than that for the smooth function. From March to September, the maximum depth at which the soil undergoes phase change (where water and ice co-exist, identified by vertical arrows in Figure 5a,b) is about 23 m for the steep freezing function (Figure 5a), whereas for the smooth function, the phase-change zone extends to the bottom boundary (Figure 5b).

As air temperatures increase during each year, the near-surface domain becomes thawed in both cases, and all pore water is left in the liquid state (Wu=1) (as shown in Figure 5a,b for

September). In this area, Case 1a with a steep freezing function is colder than Case 2a with a smooth function (Figure 5c).

In March and May after 88 years, the temperature difference between Case 1a and 2a is almost everywhere positive ($T_{\text{steep function}} > T_{\text{smooth function}}$), except for the thin shallow surface zones located at the two sides of the domain (Fig 5c), where the surface snow cover keeps the underlying ground warmer compared to the central section. In these embankment areas, the simulated temperature is slightly higher in the shallow soil assigned with a smooth freezing function compared to the system with a steep freezing function, since during the previous warmer months less energy was required to increase the shallow soil temperature with a gentle-slope freezing function (Figure 5c).

By September (Figure 5c), the shallow subsurface is everywhere colder in the soil with the steep freezing function, reaching a maximum difference of -1°C in the snow-free central portion. From March to September, in the bottom frozen zone of Case 1a (below the active layer), the temperature-depth profile (Figure 5d) is relatively uniform at about -2 °C. In contrast, the temperature in Case 2a decreases gradually with depth, from about -2 to -4 °C.

As the monthly air temperatures increase, the shallow permafrost starts to thaw. Above the -2 °C contour, soil thaw occurs faster in the case with the steep freezing function, resulting in a higher temperature at a given depth (Figure 5). However, at greater depths, temperatures are still below zero, and are generally around -2 °C for the steep freezing function and from -2 °C to -5 °C in the system assigned with a smooth freezing function.

Within the partially-thawed zone, the effects of the freezing function on the subsurface temperature distribution depend on the surface temperature variations (Figure 5). Within the deeper part of the domain, with a steeper curve (Case 1a), the deep subsurface temperatures remain around -2 °C, resulting in a relatively uniform temperature-depth profile (Figure 5d). In

comparison, with a lower slope for the freezing function (Case 2a), the deeper temperature varies over a wider range between -1 °C and -5 °C (Figure 5b,d).

3.1.2 Annual variations in the subsurface thermal regimes

Under advective-conductive heat transport (Case 2b), the evolution of temperature and the unfrozen water saturation is shown in Figure 6 for the month of September following the 88th, 178th, and 268th simulation year.

After 88 years for the month of September, the permafrost thaw front has migrated between 2-5 m into the subsurface (Figure 6a) and (in September) all water in the shallow subsurface (< 2 m below asphalt and < 10 m below snow cover) is in the liquid state (where W_u=1; Figure 6b at 88 years). The unfrozen water saturation decreases with depth, following the decrease in temperature, and reaches a minimum saturation of 0.3 close to the bottom boundary (Figure 6b at 88 years). Over the 178-year simulation under climate warming, the depth to permafrost continues to increase. By 268 years (in September), the permafrost becomes fully thawed under advective-conductive heat transport (Figure 6b).

3.1.3 Predicted depth to permafrost (thaw front)

The effect of the different freezing functions on the simulated spatial and temporal location of the thaw front throughout the domain is shown directly in the profiles of Figure 7. After 88 years under advection-controlled heat transport, the predicted thaw front depths (below the active layer) are similar for Cases 1b and 2b. With increasing mean annual air temperatures, the thaw front after 178 years has migrated slightly deeper in the case with a smooth freezing function, with a maximum difference in the depth of the thaw front of 2.6 m at the centre of the domain, where there is no snow cover. In both cases, the insulating effect of the surface snow cover at the sides of the domain allows a deeper migration of the thaw front compared to the central section.

Throughout the domain, the depth to permafrost at the end of the simulation is less for a steep freezing function, for which the thawing rate is generally slower (recall that both cases have the same porosity). With a steeper freezing function, the temperature difference is slightly greater between the (snow-free) center and the (snow-covered) sides compared to the case with a smoother freezing function. Because of the snow cover, subsurface temperatures at the sides in the case with a steep freezing function have already increased, analogous to the case with a smooth freezing function, resulting in a greater thickness of the thawed zone, below the active layer, compared to the center. Thus, over the same time interval, the thawing rate at the colder, snow-free centre of the domain in the steep freezing function case will be even slower, resulting in a maximum difference after 178 years of 2.6 m in the predicted depth to permafrost compared to the case with a smooth freezing function. This behaviour is expected since over the same time interval, a greater amount of energy is required to increase the soil temperature near the colder center compared to the sides.

As the air temperature increases further from 178 years to 268 years, deeper subsurface temperatures also increase, leading to an almost complete thaw (below the active zone) for the case with a smooth freezing function. At the same time, the case with a steep freezing function remains ice-rich and only partly thawed.

After 268 years under conductive heat transport alone, the maximum difference in the depths to permafrost between the two cases is 17.5 m (Cases 1a, 1b). When the system with a smooth freezing function is almost completely thawed, permafrost still exists in the deeper layers of the soil with a steep freezing function. This is due to the lower residual unfrozen moisture content in the steep freezing function case, resulting in a greater volume of ice which requires more energy to melt.

The effects of the two different freezing functions assuming advective-conductive heat transfer (Cases 1b,2b) are also depicted in Figure 7. After 268 years, the permafrost becomes completely thawed in the advective-conductive system with a smooth freezing function, and the difference between the conduction and advection-controlled systems is only apparent in the center. In contrast, the soil with a steep freezing function under advection-conduction is not yet fully thawed after 268 years, and the difference between conduction and advection in this case becomes slightly greater at the left side of the domain, as the thawed zone penetrates deeper into the ground.

The simulated temperatures for the first 20 years for Cases 1a and 2a are illustrated in Figure 8 at two locations. Point 1 is about 1.5 m below the right embankment (48.5 m elevation) and Point 2 is about 4.5 m below the left embankment (45.5 m elevation), (see locations in Figure 2). As the soil freezes due to decreasing surface air temperatures over each fall and winter, the maximum temperature difference between the two cases at Point 1 occurs at the seasonal minimum temperatures at which the soil is completely frozen. The maximum average difference is about -3 °C over the 20-year time period, with the soil having a steep freezing function, Case 1a, being colder than that with a smooth freezing function, Case 2a (Figure 8a). As the soil thaws due to increasing air temperatures each spring, the maximum difference between the two cases at Point 1 occurs at the maximum extreme points of the profile, where Case 1a has a higher temperature compared to Case 2a.

At the deeper monitoring location at Point 2 (below a winter snow cover), the temperature changes occur more slowly in the soil with a smooth freezing function. Temperature extremes are also much more attenuated relative to the soil with a steep freezing function (Figure 8b). The maximum temperature difference between the two cases at Point 2 occurs where the ice fraction in the soil with a smooth freezing function is melting and where the soil with a steep function is

still completely frozen. The temperature difference is greatest at this state since complete phase change with the steep freezing function occurs between 0°C and -2°C while for the smooth function the phase change occurs between 0 °C and -6°C (see Eq. 5, and Figure 4).

At Point 2, the soil with a steep freezing function remains frozen at all times (since $T < -2$°C), while the soil with a smooth function undergoes partial phase change (since $T > -6$°C). At the shallower depth of 1.5 m (Point 1), both soils undergo phase change, due to their proximity to surface temperature variations (Figure 8a).

3.2 Effects of soil heterogeneity

The thermal behaviour of the homogeneous system, Cases 2a-b, as a function of both hydraulic and thermal properties, is compared to a heterogeneous system, Cases 3a-b, under conduction only (Case 2a, 3a) and under advective-conductive heat transport (Case 2b, 3b). The relative permeability and thermal conductivity are allowed to vary in space and time depending on the temperature (and hence ice-fraction) evolution.

In Cases 3a and 3b, the heterogeneous hydraulic conductivity and porosity fields were generated using the FGEN (**F**ield **Gen**erator) code (Robin et al. 1993) with a log-mean hydraulic conductivity and mean porosity identical to the homogeneous soil, Case 2, (2×10^{-5} m s^{-1} and 0.34, respectively; Table 1). A log K variance of σ^2=0.5 was used with horizontal and vertical correlation lengths (λ_x and λ_z) of 10 m and 2 m, respectively. The resulting (fully thawed) K field varies from 10^{-6} m s^{-1}, representative of finer-grained material, to a maximum of about 10^{-4} ms^{-1}, representative of a coarse-grained material (Figure 9a).

The stochastic porosity distribution was generated assuming an inverse correlation with hydraulic conductivity. A porosity variance of σ^2=0.016 was used with correlation lengths (λ_x and λ_z) of 10 m and 2 m, respectively. The generated porosity field varied from a maximum of 0.5,

representative of finer-grained material, to a minimum of about 0.2, representative of a coarse-grained material (Figure 9b). The initial thermal conductivity distribution, which depends on the porosity and temperature, is shown in Figure 9c.

The heterogeneous simulations were run under the same climate change scenario as the previous homogeneous case, over 268 years and assuming a smooth freezing function, until the permafrost had completely thawed in both cases. Over the 268-year simulation, the temperature distribution and unfrozen water saturation for Case 3b (heterogeneous, advection-conduction) were similar to those for Case 2b (homogeneous, advection-conduction) in Figure 6, and are therefore not shown.

3.2.1 Evolution of unfrozen flow system

The spatial and temporal evolution of groundwater flow for the homogeneous and heterogeneous cases are compared after 88, 178, and 268 years in Figure 10a,b, together with the corresponding evolution of hydraulic conductivity (Figure 10c,d). As the thaw front propagates downward over time, the active flow system also increases in depth, reaching the full domain thickness by 268 years (Figure 10a). In the heterogeneous case, the flow system is much more irregular, following the stochastic K field, and converging within higher K zones. Nevertheless, the general behaviour is similar, with the active flow system advancing over time at about the same rate (Figure 10a,b).

As the thaw front migrates deeper, the pore ice melts which increases both the unfrozen water saturation (Wu in Equation 5) and the relative permeability (k_r in Equation 6). This increase is most visible for the homogeneous case (Fig 10c). Although a clear thaw front indicated by the k_r=1 contour is not apparent in the heterogeneous case (Figure 10d), a general increase in relative permeability with depth is nevertheless still seen.

3.2.2 Conduction versus advection-conduction

Differences in the ground thermal regime between the heterogeneous and homogeneous systems, under conduction only (Case 2a, 3a) and advection-controlled heat transport (Case 2b, 3b), can be highlighted by inspecting the predicted depths to permafrost at different times (Figure 11). After 88 years, the predicted depth to permafrost for all cases is quite similar along the transect, and the maximum depth to permafrost at the sides is about 6 m in both cases. Although the shallow flow system is active (unfrozen) for all cases, thermal conduction is the main driver for permafrost thaw and the effect of advective thermal transport is negligible at this early time (after 88 years).

After 178 years, the conduction-only cases (2a, 3a) and advective-conductive cases (2b, 3b) yield slightly different depths to permafrost, primarily from the left side to the center, where the predicted permafrost depth under advective-conductive heat transport is 2 m deeper compared to conduction only. After 208 years, the difference between conductive and advective-conductive heat transport in these two cases has grown at the left (upgradient) and central portions of the domain due to advective heat transport. The depth to permafrost at the left (below the main recharge area) is clearly deeper in the advection-conduction case relative to the conduction-only case. However, to the right (downgradient), the predicted depth to permafrost under advection-conduction is slightly shallower compared to that for conductive heat transport only. At this simulation time, the maximum difference in the predicted depths to permafrost is about 3 m greater with advective-conductive heat transport compared to conduction only (very close to the left boundary), in both the homogeneous and heterogeneous cases. The simulated permafrost depth at 208 years under advective-conductive heat transport is 1.5 m deeper for the heterogeneous case compared to the homogeneous case.

After 238 years, in addition to conductive heat transport, advection also contributes to further degradation of permafrost, specifically in the left (upgradient) part of the domain where vertical recharge is most significant. Here, the greater penetration of warmer temperatures in both cases shows that advection plays an increasingly important role in heat transfer, with groundwater flowing from the recharge area at the left side of the domain to the discharge boundary on the right. The thaw rate is slightly faster in the heterogeneous case with advective heat transport, due to the more hydraulically conductive zones. As groundwater flows through the system just above the permafrost table and approaches the right boundary, heat is lost to the cooler soil and underlying permafrost. In the downgradient zone, the predicted temperatures under advection-conduction are thus slightly lower compared to temperatures predicted by conductive heat transport alone (Figure 11, 238 years) reflecting a negative (inverse) feedback between advection and permafrost thaw. This negative feedback effect was already seen as early as 178 years (Figure 11) and is contrary to the expectation that advective heat transport from flowing groundwater always enhances permafrost thaw (positive feedback). Positive feedback is indeed seen in the upgradient area, where the thaw depth under advective-conductive heat transport is greater due to infiltration of warmer water.

In the downgradient zone of the homogeneous system, the predicted temperatures under advection-conduction are also slightly lower compared to temperatures predicted by conductive heat transport alone (Figure 11, 208 and 238 years). Thus, the negative feedback between advection and permafrost thaw occurs in both homogeneous and heterogeneous cases.

After 238 years, the maximum depth to permafrost in the heterogeneous case is predicted to be 2.6 m deeper than in the homogeneous case, under advective-conductive heat transport. The permafrost depth at the right side and the central portion of the domain is similar in both cases, despite the differences in hydraulic conductivity and porosity. After 238 years, the simulated

depth to permafrost for both the homogeneous /heterogeneous cases is deeper under advection-conduction compared to conduction-only heat transport, generating a maximum difference of about 6 m.

After 268 years, permafrost has completely thawed under advective-conductive heat transport within the homogeneous and heterogeneous domains (Cases 2b-3b), in contrast to conductive heat transport only (Cases 2a-3a), in which the permafrost persists longer (Figure 11). After 268 years under conduction only, the depth to permafrost in the heterogeneous case is about 7 m deeper than in the equivalent homogeneous case. This deeper active zone in the heterogeneous case is related to its lower porosity areas (with a higher thermal conductivity), allowing a greater penetration of heat into the ground via conductive heat transfer.

4 Discussion

As the numerical simulations show, permafrost response to climate change depends on several hydrogeological and environmental factors, including the depth of the groundwater flow system, soil heterogeneities which create preferential flow, the shape of the freezing function, and snow accumulation. The predicted sensitivity of permafrost to changes in hydrogeological parameters is consistent with results from other coupled groundwater flow and heat transport models. For example, McKenzie et al. (2007) also showed how the shape of the freezing function influences the rate and extent of ice formation and that a greater amount of latent heat released over a smaller temperature range can delay migration of the freezing front. Kurylyk et al. (2014b) showed that neglecting latent heat during pore-ice thaw can over-estimate the depth of the active layer.

In the above-mentioned studies, the sensitivity of the shape of the freezing function was evaluated by applying solutions of the Lunardini and Neumann problems. In comparison, the present study considered permafrost degradation at a real field site, below a cold-region partially-paved terrain under climate warming. Simulations show that as surface temperatures change over time, the type of freezing function chosen for a system plays an important role in changing the thermal regime of the frozen ground. For example, as the seasonal surface temperature oscillates, the thawing and freezing rates will vary depending on the freezing function (Figure 8). The behaviour is linked to the latent heat adsorbed or expelled during phase change, which depends on the slope of the freezing function (Equation 5). Within the respective phase change regions (-6 °C < T < 0 °C for a smooth freezing function and -2 °C < T < 0 °C for a steep function), the latent heat released or absorbed will be greater in a soil with a steeper function compared to a soil with a smooth function (neglecting any differences in porosity and assuming the smooth function also has a higher residual unfrozen moisture saturation). Thus, over the same time interval, the temperature will change more slowly in a case with a steep freezing function, compared to a soil with a lower slope freezing function. The vertical extent of the phase-change zone is also less in a system with a steeper function and lower residual unfrozen water saturation, compared to that with a smooth freezing function where the phase-change zone occupies almost the whole domain (Figure 5a,b).

As the soil temperature decreases, where both soils become completely frozen, a soil with a lower residual unfrozen water saturation will result in a lower temperature compared to a system with a higher residual water saturation (the minimum extreme points of the profile in Figure 8a). This is due to the higher thermal conductivity of ice compared to water. Thus, in a completely frozen state, a soil with a lower residual unfrozen water saturation will result in a lower temperature.

The difference between the various freezing functions in predicting the depth to permafrost is significant. In particular, the shallow subsurface thaws faster in a soil with a smooth freezing function and higher residual unfrozen water saturation than in a soil with a steep freezing function, since less latent heat energy is required to increase the subsurface soil temperature (Figure 7). In addition, as the thaw front deepens more rapidly in the case with a smooth freezing function, the contribution of advective heat transport to permafrost thaw also increases, inducing a positive feedback in the recharge area. A deeper thawed zone (below the active layer) and a greater vertical extent of the phase-change zone due to the lower slope freezing function, (assuming the same porosity and permeability), will increase groundwater flow in the system.

Together with increasing air temperatures due to climate or seasonal changes, the presence of a snow cover in colder months accelerates the permafrost thaw rate due to its insulation effect, acting as a barrier against heat loss from the warmer subsurface to the colder ground surface (Shojae Ghias et al. 2015, 2016). In the current simulations, this insulating effect is evident from the temperature distribution in the homogeneous case (Figure 6a), where despite the uniform soil properties, the downward propagation of the thaw-front is not laterally uniform, being greater at the sides due to the presence of the snow cover, compared to the snow-free central portion.

The role of thermal advection in exacerbating permafrost thaw has been investigated numerically by several researchers (e.g., McKenzie and Voss, 2013; Rowland, 2011; Wellman et al. 2013). These studies have shown that advective heat transport due to groundwater flow can significantly increase permafrost thaw. In contrast, however, the present study found that advective heat transport can in some cases temporarily (and paradoxically) *increase* the permafrost table in downgradient areas where the flowing cold water negates heat gain from vertical conduction alone (Figure 11 at 208 and 238 years). Knowledge of the specific hydrogeological setting and material properties is critical for the assessment of advective heat

transport in permafrost environments, as suggested by Shojae Ghias et al. (2016). This current study reveals that accounting for high-permeability zones in a heterogeneous soil, where relatively warm water infiltrates as recharge, also enhances thermal advection.

The effects of groundwater flow and advective heat transport are particularly evident in the homogeneous system after 178 years, where the thaw front is asymmetric along the transect, being deeper at the left side of the domain compared to the right side (Figure 11, for $t \geq 178$ years). Asymmetry develops because groundwater recharging at the top left of the domain tends to flow vertically through the high permeability soil, before flowing generally horizontally toward the right discharge boundary. In addition, when groundwater reaches the right boundary, it is no longer warm enough to induce further thaw by advection (ex. Figure 11 at 238 years), due to loss of heat to the underlying permafrost along the upgradient flowpath. In fact, this cold water keeps the downgradient area colder than under conductive heat transport alone and leads to a short-term increase in the permafrost table in both the homogeneous and heterogeneous cases. This result is counter-intuitive since advection is usually associated with influx of warmer water and accelerating permafrost thaw. While in all cases under conductive heat transport alone, the permafrost persists beyond the maximum simulation time of 268 years, by this time under advective-conductive heat transport, the permafrost has completely disappeared.

5 Conclusion

The simulations investigated the effect of the freezing function and soil heterogeneity on permafrost thaw for a warming climate. The results show that the shape factor (controlling the slope of the freezing function) and the residual unfrozen water saturation play important roles on

the spatial and temporal temperature distribution in a permafrost setting subject to annual freezing and thawing cycles. With a steeper curve, the permafrost table will be shallower compared to that for a smooth freezing curve. The time required for permafrost to completely thaw will therefore increase for a soil with a steeper freezing function and a lower residual unfrozen water saturation. Also, as the slope of the freezing function decreases, the importance of thermal advection on the ground thermal regime will generally increase as the active zone thickness increases leading to deeper infiltration of recharge. Under frequent ground freezing and thawing due to air temperature fluctuations, choosing the appropriate freezing function (based on the soil type), is therefore important for ensuring more physically realistic numerical models of permafrost.

The simulation results also reveal the importance of the hydraulic conductivity field in controlling groundwater flow within a permafrost environment, as well as the importance of the porosity distribution in controlling conductive heat transport. High-permeability zones in a heterogeneous soil within a recharge area with infiltration of relatively warm water would increase thermal advection, and over the long term the predicted depth of the thaw front would be relatively greater compared to a homogeneous system with a uniform hydraulic conductivity. Also, low porosity zones (with a corresponding higher thermal conductivity) in a heterogeneous system induce a deeper thaw front compared to the homogeneous system.

Therefore, in contrast to the expectation that advection will always transfer heat into a system and intensify permafrost degradation, a negative feedback can also develop in downgradient flow zones of both homogeneous and heterogeneous systems which will reduce the thaw rate and can indeed, at least over the short term near a discharge zone, lead to a higher permafrost table than that formed by vertical conductive heat transport only.

The simulations have nevertheless shown that, for a given conceptual model, permafrost will generally persist longer in systems controlled by thermal conduction compared to those under advective-conductive heat transport. This applies to both homogeneous and heterogeneous systems. The simulated homogeneous and heterogeneous systems show that in recharge areas where relatively warm water is infiltrating toward permafrost, advective heat transport is the primary contributor to permafrost thaw.

The results have provided insight into permafrost dynamics in response to hydrogeological factors under climate warming and have highlighted those parameters and processes which must be well characterized in the field to increase reliability of coupled groundwater-permafrost models.

Acknowledgments

We would like to thank the Geological Survey of Canada (Ministry of Natural Resources Canada) for their financial support and access to the site and data. This study was also financed in part by Discovery Grants to Dr. R. Therrien, Dr. J. Molson and Dr. J-M. Lemieux from the Natural Sciences and Engineering Research Council of Canada (NSERC). Pierre Therrien of Université Laval provided technical assistance with the computational work which is gratefully acknowledged.

References

Andersland, O.B., and Anderson, D.M. 1978. Geotechnical Engineering for Cold Regions. McGraw-Hill Book, Co., New York, N.Y.

Andersland, O.B., and Ladanyi, B. 2004. Frozen Ground Engineering. John Wiley and Sons, Hoboken, N.J.

Bense, V.F., Kooi, H., Ferguson, G., and Read, T. 2012. Permafrost degradation as a control on hydrogeological regime shifts in a warming climate. Journal of Geophysical Research, **117**: F03036. doi:10.1029/2011JF002143.

Carslaw, H.S., and Jaeger, J.C. 1959. Conduction of Heat in Solids. 2nd Edition, Oxford University Press, Oxford, U.K.

Farouki, O.T. 1981. Thermal Properties of Soil. U.S. Army Corps of Engineering, CRREL Monograph 81–1, Cold Regions Research and Engineering Laboratory, Hanover, N.H.

Fortier, R., LeBlanc, A., and Wenbing, Y. 2011. Impacts of permafrost degradation on a road embankment at Umiujaq in Nunavik (Quebec), Canada, Canadian Geotechnical Journal, **48**(5): 720–740. doi:10.1139/t10-101.

Freeze, R.A., and Cherry, J.A. 1979. Groundwater. Prentice-Hall, Inc., Englewood Cliffs, N.J.

Ge, S., McKenzie, J., Voss, C.I., and Wu, Q. 2011. Exchange of groundwater and surface-water mediated by permafrost response to seasonal and long term air temperature variation. Geophysical Research Letters, **38**: L14402. doi:10.1029/2011GL047911.

Grenier, C., Anbergen, H., Bense, V., Chanzy, Q., Coon, E., Collier, N., Costard, F., Ferry, M., Frampton, A., Frederick, J., Holmen, J., Jost, A., Kokh, S., Kurylyk, B., McKenzie, J., Molson, J., Mouche, E., Orgogozo, L., Pannetier, R., Rivière, A., Roux, N., Rühaak, W., Scheidegger, J., Selroos, J.O., Therrien, R., Vidstrand, P., and Voss, C. 2018. Groundwater flow and heat transport for systems undergoing freeze-thaw: Intercomparison of numerical

simulators for 2D test cases, Advances in Water Resources, **114**:196–218, doi:10.1016/j.advwatres.2018.02.001.

Heath, R.C. 1983. Basic Ground-water Hydrology. U.S. Geological Survey Water-Supply Paper 2220, Reston, Virginia, U.S.

IPCC. 2007. Contribution of working groups I, II and III to the fourth assessment report of the intergovernmental panel on climate change. Core writing team, Pachauri, R.K., Reisinger, A., IPCC, Geneva, Switzerland.

Jame, Y.W., and Norum, D.I. 1980. Heat and mass transfer in freezing unsaturated porous media. Water Resources Research, **16**(4): 811–819. doi: 10.1029/WR016i004p00811.

Kane, D.L., Hinkel, K.M., Goering, D.J., Hinzman, L.D., and Outcalt, S.I. 2001. Non-conductive heat transfer associated with frozen soils. Global and Planetary Change, **29**(3): 275–292. doi:10.1016/S0921-8181(01)00095-9.

Kurylyk, B.L., MacQuarrie, K.T.B., and Voss, C.I. 2014. Climate change impacts on the temperature and magnitude of groundwater discharge from shallow, unconfined aquifers. Water Resources Research, **50**(4): 3253–3274. doi: 10.1002/2013WR014588.

Kurylyk, B.L., MacQuarrie, K.T.B., and McKenzie, J.M. 2014. Climate change impacts on groundwater and soil temperatures in cold and temperate regions: implications, mathematical theory and emerging simulation tools. Earth-Science Reviews. **138**: 313–334. doi: 10.1016/j.earscirev.2014.06.006.

Kurylyk, B.L., McKenzie, J.M., MacQuarrie, K.T.B., and Voss, C.I. 2014. Analytical solutions for benchmarking cold regions subsurface water flow and energy transport models: one dimensional soil thaw with conduction and advection. Advances in Water Resources. **70**: 172–184. doi: 10.1016/j.advwatres.2014.05.005.

LeBlanc, A.M., Oldenborger, G.A., Sladen, W.E., and Allard, M. 2015. Infrastructure and climate warming impacts on ground thermal regime, Iqaluit International Airport, southern Baffin Island, Nunavut. Summary of Activities 2014, Canada-Nunavut Geoscience Office, pp. 119–132.

Ling, F., and Zhang, T. 2003. Impact of the timing and duration of seasonal snow cover on the active layer and permafrost in the Alaskan Arctic. Permafrost and Periglacial Processes, **14**: 141–150. doi: 10.1002/ppp.445.

Lunardini, V.J. 1985. Freezing of soil with phase change occurring over a finite temperature difference. *In* Proceedings of the 4th International Offshore Mechanics and Arctic Engineering Symposium, American Society of Mechanical Engineers, pp. 38-46.

Lunardini, V.J. 1991. Heat Transfer with Freezing and Thawing, Elsevier Science, New York, N.Y.

McKenzie, J.M., Voss, C.I., and Siegel, D.I. 2007. Groundwater flow with energy transport and water–ice phase change: numerical simulations, benchmarks, and application to freezing in peat bogs. Advances in Water Resources. **30**(4): 966–983. doi:10.1016/j.advwatres.2006.08.008.

McKenzie, J.M., and Voss, C.I. 2013. Permafrost thaw in a nested groundwater-flow system. Hydrogeology Journal, **21**(1): 299–316. doi: 10.1007/s10040-012-0942-3.

Molson, J.W., and Frind, E.O. 2017. HEATFLOW-SMOKER: Density-dependent flow and advective-dispersive transport of thermal energy, mass or residence time. University of Laval and University of Waterloo, pp. 116.

Palmer, C.D., Blowes, D.W., Frind, E.O., and Molson, J.W. 1992. Thermal energy storage in an unconfined aquifer: 1. Field injection experiment, Water Resources Research, **28**(10): 2845–2856. doi:10.1029/92WR01471.

Robin, M.J.L., Gutjahr, A.L., Sudicky, E.A., and Wilson, J.L. 1993. Cross-correlated random-field generation with the direct Fourier Transform method, Water Resources Research, **29**: 2385–2397. doi: 10.1029/93WR00386.

Roosmalen, L.V., Christensen, B.S.B., and Sonnenborg, T.O. 2007. Regional differences in climate change impacts on groundwater and stream discharge in Denmark. Vadose Zone Journal, **6**(3): 554–571. doi: 10.2136/vzj2006.0093.

Rowland, J.C., Travis, B.J., and Wilson, C.J. 2011. The role of advective heat transport in talik development beneath lakes and ponds in discontinuous permafrost. Geophysical Research Letters, **38**: L17504. doi:10.1029/2011GL048497.

Rühaak, W., Anbergen, H., Grenier, C., McKenzie, J., Kurylyk, B.L., Molson, J., Roux, N., and Sass, I. 2015. Benchmarking numerical freeze/thaw models. Energy Procedia, **76**: 301–310. doi :10.1016/j.egypro.2015.07.866.

Serreze, M.C., Walsh, J.E., Chapin III, F.S., Osterkamp, T., Dyurgerov, M., Romanovsky, V., Oechel, W.C., Morison, J., Zhang, T., and Barry, R.G. 2000. Observational evidence of recent change in the northern high-latitude environment. Climatic Change, **46**:159–207. doi:10.1023/A:1005504031923.

Shojae Ghias, M., Therrien, R., Molson, J., and Lemieux, J.M. 2015. Numerical simulations of coupled groundwater flow and heat transport incorporating freeze/thaw cycles and phase change in a continuous permafrost environment. *In* Proceedings of GeoQuebec 2015 conference, 68th Canadian Geotechnical Conference and 7th Canadian Permafrost Conference, Canadian Geotechnical Society, 21-23 September 2015, Quebec City, pp. 8.

Shojae Ghias, M., Therrien, R., Molson, J., and Lemieux, J.M. 2017. Controls on permafrost thaw in a coupled groundwater flow and heat transport system: Iqaluit Airport, Nunavut, Canada. Hydrogeology Journal, **25**(3): 657–673, doi:10.1007/s10040-016-1515-7.

Watanabe, K., Kito, T., Wake, T., and Sakai, M. 2011. Freezing experiments on unsaturated sand, loam and silt loam. Annals of Glaciology, **52**(58): 37–43. doi: 10.3189/172756411797252220

Wellman, T.C., Voss, C.I., and Walvoord, M.A. 2013. Impacts of climate, lake size, and supra and sub-permafrost groundwater flow on lake-talik evolution, Yukon Flats, Alaska (USA). Hydrogeology Journal, **21**(1): 281–298. doi: 10.1007/s10040-012-0941-4.

Zhang, T., Barry, R.G., Knowles, K., Ling, F., and Armstrong, R.L. 2003. Distribution of seasonally and perennially frozen ground in the Northern Hemisphere. Edited by Phillips, Springman and Arenson. Permafrost, Balkema Publishers, Leiden, pp. 1289–1294.

Zhang, Y., Chen, W., and Riseborough, D.W. 2008. Transient projections of permafrost distribution in Canada during the 21st Century under scenarios of climate change, Global and Planetary Change, **60**(3): 443–456. doi: 10.1016/j.gloplacha.2007.05.003.

Figure Captions

Figure 1. Site location maps showing a) Location of Iqaluit Airport, Nunavut, Canada (63.45° N and 68.33° W) which is used as a reference to develop the conceptual model in this study (Figure 2), and (b) Taxiway Alpha; the approximate model region is indicated by the circle.

Figure 2. Hydrogeological conceptual model with boundary conditions for groundwater flow and heat transport.

Figure 3. Annual mean air temperatures (black line), maximum mean monthly air temperatures (red line) and minimum mean monthly air temperatures (blue line) predicted for the 2013-2280 period at the Iqaluit Airport.

Figure 4. Unfrozen water saturation as a function of temperature using a steep freezing function (Case 1a,b) and a smooth (low slope) freezing function (Case 2a,b). See Equation 5 and Table 2 for parameter definitions.

Figure 5. Simulated temperature distributions for a) Case 1a (homogeneous system, steep freezing function) and b) Case 2a (homogeneous system with a smooth freezing function), for March, May and September after 88 years; conductive heat transport only. The temperature difference between these two cases, and the corresponding vertical profiles (at x=73 m), are shown in (c) and (d), respectively. The vertical arrows identify the phase-change regions where water and ice co-exist.

Figure 6. Thermal behaviour resulting from advective-conductive heat transport in the homogeneous system, with a smooth freezing function, under climate warming, showing a) ground temperatures, and b) the respective corresponding evolution of unfrozen water saturation. The simulation results are plotted for the month of September after the 88th, 178th, and 268th year. The dashed lines show the location of the thaw front (0 °C).

Figure 7. Simulated spatial and temporal locations of the depth to permafrost (thaw front below the active layer) using different freezing functions in a homogeneous system, for cases with a steep freezing function (Case 1a,b) compared to a gentle function (Case 2a,b), over 268 years under conductive (solid line) and advective-conductive (symbols) heat transport. The blue arrows show the maximum difference in depth to permafrost between the two conduction-only cases after 178 and 268 years.

Figure 8. Temperature changes over time (0-20 years) at monitoring points 1 and 2 ((a) and (b), respectively; see locations in Figure 2), using a steep freezing function and smooth freezing function as shown in Figure 4 and defined in Table 2. Point 1 is about 1.5 m below the right embankment (at 48.5 m elevation) and Point 2 is about 4.5 m below the left embankment (at 45.5 m elevation). The temperature differences between the two soil cases, at each monitor point, are shown as a dashed pink line.

Figure 9. Heterogeneous Cases 3a,b: a) initial stochastic *K* field (log K m s_{-1}), b) the inversely-correlated porosity distribution, and c) the initial thermal conductivity distribution. See Table 1 for stochastic parameters.

Figure 10. Temporal and spatial evolution of the simulated flow systems (equipotentials and flow paths), resulting from a) a homogeneous soil and b) a heterogeneous system, and c-d) the respective evolution of hydraulic conductivity, under the future climate scenario for Cases 2b and 3b, respectively.

Figure 11. Simulated spatial and temporal distribution of the depth to permafrost comparing the completely homogeneous soil (Case 2a,b) to a heterogeneous soil with a stochastic K and porosity field (Case 3a,b), under conduction-only and advective-conductive driven thaw, based on the climate scenario over 88, 178, 208, 238 and 268 years. Vertical black arrows identify the maximum differences in depth to permafrost between the homogeneous and heterogeneous cases under advection-conduction while the red arrow identifies the corresponding maximum difference under conduction alone after 268 years.

Table 1. Soil characteristics for the homogeneous and heterogeneous cases. The porosity as well as the hydraulic and thermal conductivities from the homogeneous case were used as mean values in the heterogeneous case. In all cases, the bulk effective thermal conductivity and hydraulic conductivity depend on the temperature.

Structural unit (homogeneous; Case 1-2)	Porosity (-)	Density of solid grains ($kg\ m^{-3}$)	Thermal conductivity of solid grains ($J\ m^{-1}\ s^{-1}\ °C^{-1}$)	Specific heat of solid grains ($J\ kg^{-1}\ °C^{-1}$)	Hydraulic conductivity ($m\ s^{-1}$)
Unit 1	0.34[a]	2650[b]	2.9[b]	732.7[b]	2×10^{-5} [c]
Asphalt layer	10^{-3}	2100[d]	1.51[d]	976[d]	10^{-10}
Structural unit (heterogeneous; Case 3)	**Mean porosity (-)**	**Mean hydraulic conductivity ($m\ s^{-1}$)**	**Variance for porosity (σ^2)**	**Variance for hydraulic conductivity (σ^2)**	**Correlation lengths (m) for porosity and hydraulic conductivity (λ_x, λ_z)**
Unit 1	0.34[a]	2×10^{-5} [c]	0.5	0.016	10, 2

[a] Freeze and Cherry (1979), [b] Farouki (1981), [c] Heath (1983), [d] Andersland and Anderson (1978).

Table 2. Physical and numerical model parameters used for the simulation scenarios.

Model Parameters	**Value**
Water and ice physical properties	
Density of water (at 4 °C) [a]	1000 kg m^{-3}
Density of ice	920 kg m^{-3}
Water thermal conductivity	0.58 J m^{-1} s^{-1} $ºC^{-1}$
Ice thermal conductivity	2.14 J m^{-1} s^{-1} $ºC^{-1}$
Water specific heat	4187 J kg^{-1} $ºC^{-1}$
Ice specific heat	2108 J kg^{-1} $ºC^{-1}$
Latent heat of fusion	334,000 J kg^{-1}
Freezing function and relative permeability	
Freezing function $W_u(T)$	$W_u(T) = (1-p)\cdot e^{(-(T/q)^2)} + p$
Curvature of freezing function *(q)*	Smooth: 3.0, Steep: 1.0
Terminal unfrozen moisture content *(p)*	Smooth: 0.2, Steep: 0.1
Relative permeability function $k_r(T)$	$k_r(T) = \max\left[10^{-\Omega\cdot\theta(1-Wu(T))}, 10^{-6}\right]$
Empirically derived impedance factor (Ω)	10.0

[a] See Molson and Frind (2017) for temperature-dependent density and viscosity functions.

Table 3. Description of the simulation scenarios with associated cases.

Case description
Homogeneous; steep freezing function Case 1a- Conduction only Case 1b- Advection-conduction
Homogeneous; smooth freezing function Case 2a- Conduction only Case 2b- Advection-conduction
Heterogeneous system Case 3a- Conduction only Case 3b- Advection-conduction

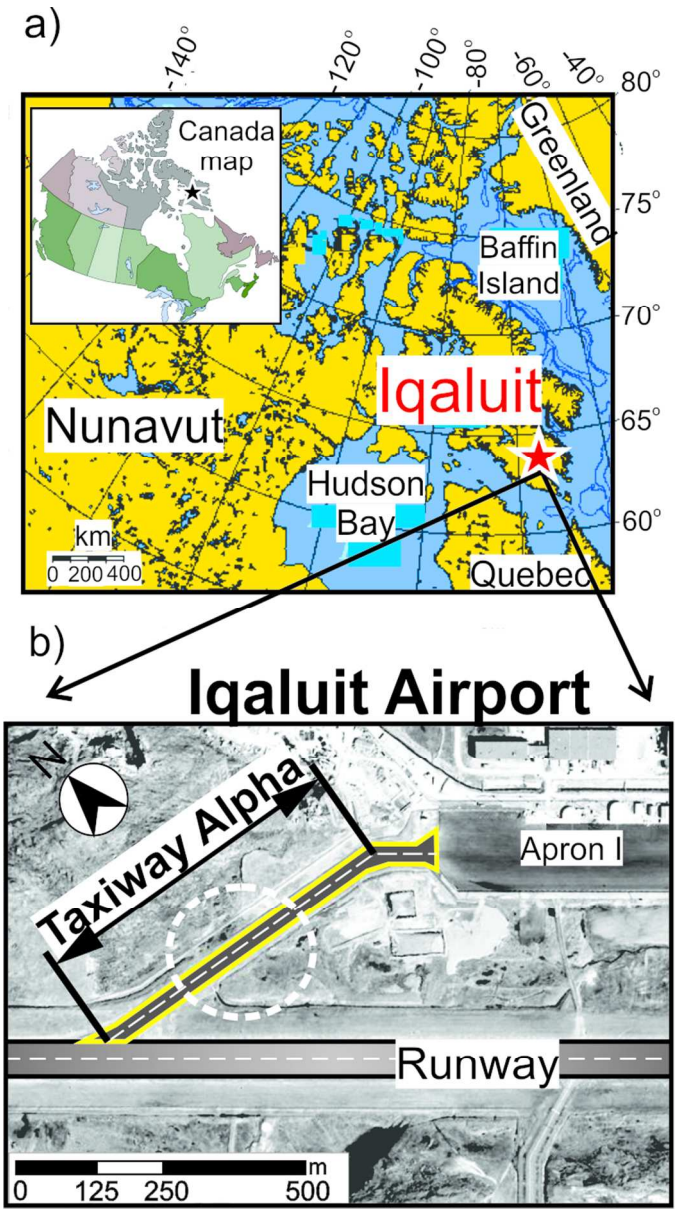

Figure 1. Site location maps showing a) Location of Iqaluit Airport, Nunavut, Canada (63.45° N and 68.33° W) which is used as a reference to develop the conceptual model in this study (Figure 2), and (b) Taxiway Alpha; the approximate model region is indicated by the circle.

68x123mm (300 x 300 DPI)

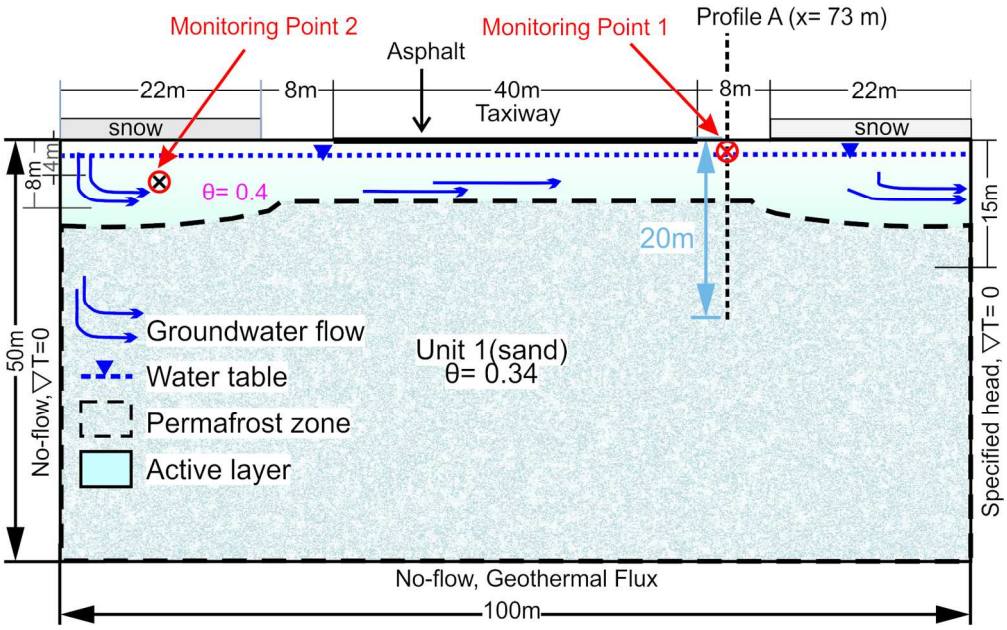

Figure 2. Hydrogeological conceptual model with boundary conditions for groundwater flow and heat transport.

151x97mm (300 x 300 DPI)

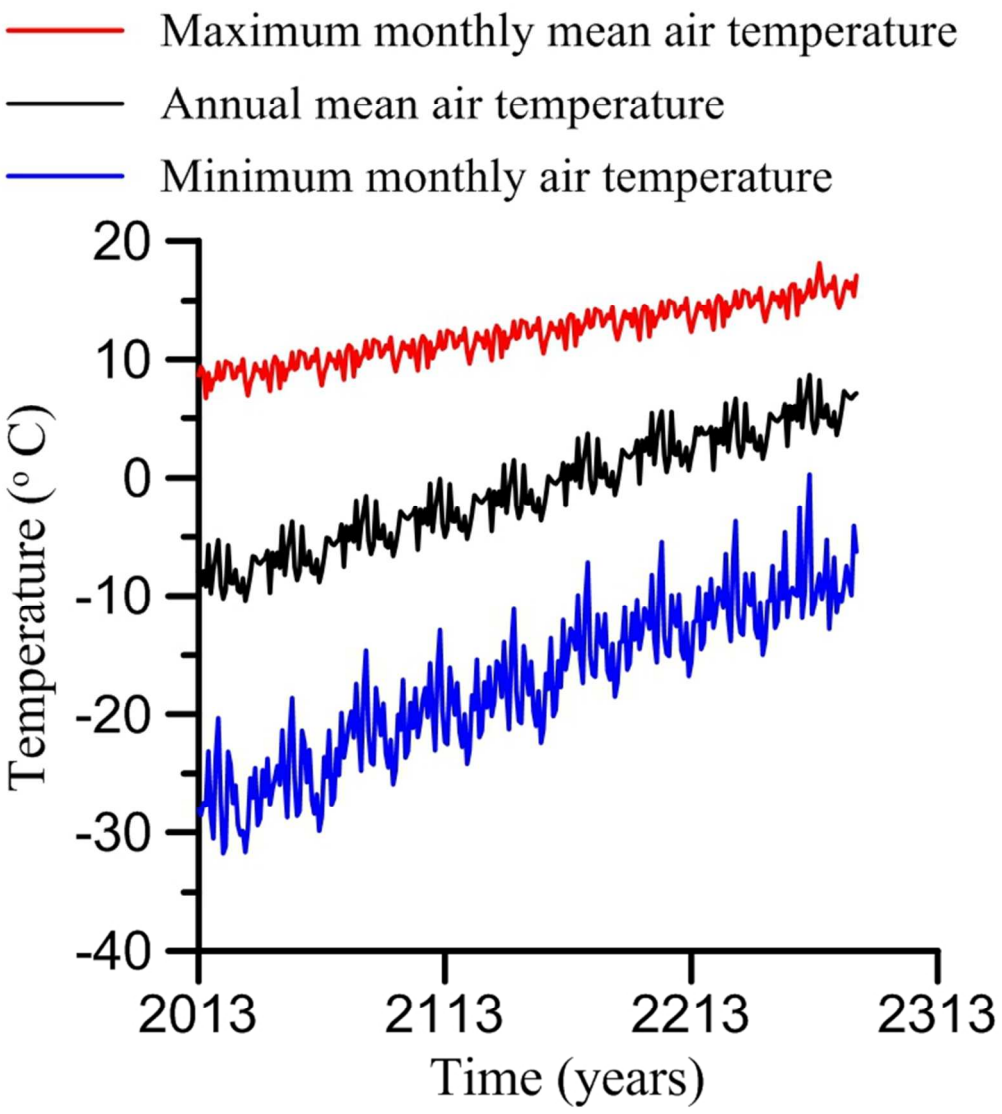

Figure 3. Annual mean air temperatures (black line), maximum mean monthly air temperatures (red line) and minimum mean monthly air temperatures (blue line) predicted for the 2013-2280 period at the Iqaluit Airport.

65x72mm (299 x 299 DPI)

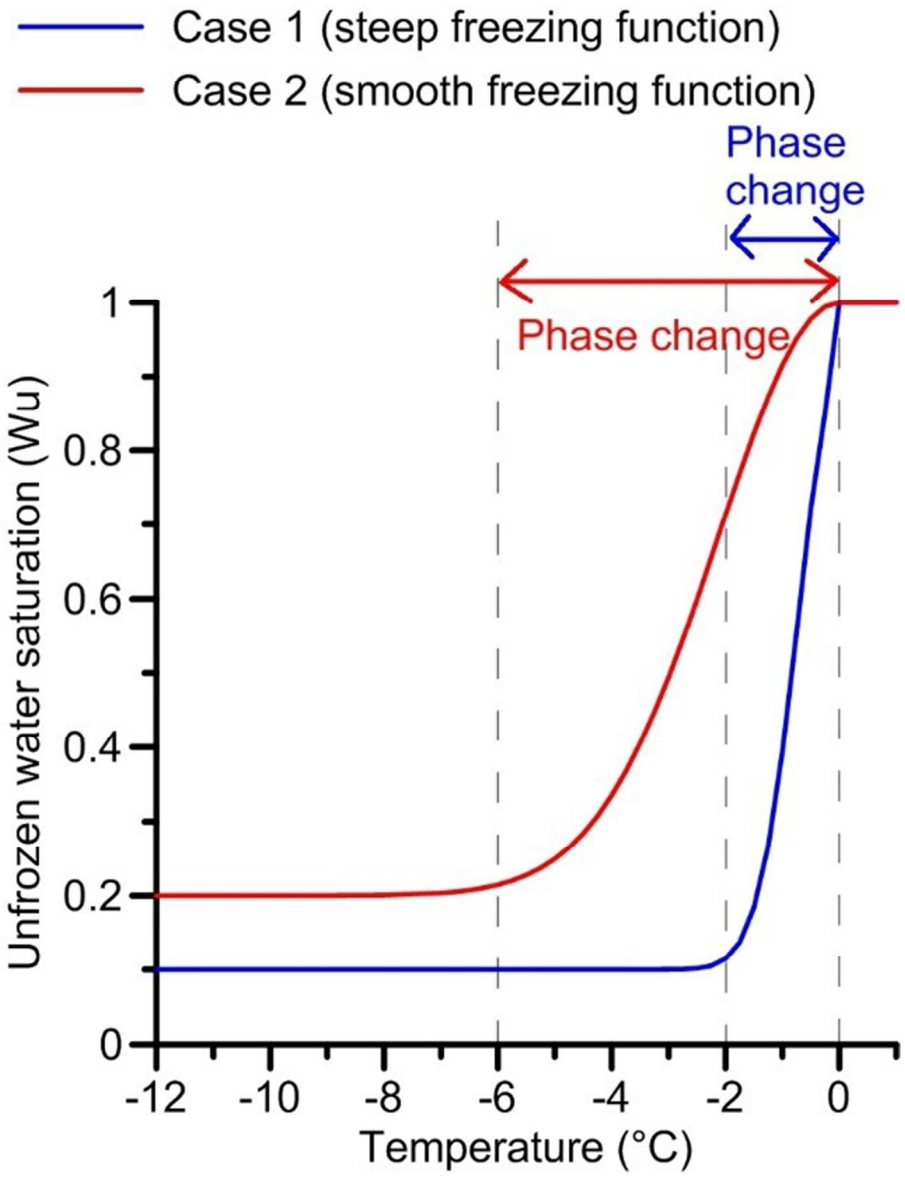

Figure 4. Unfrozen water saturation as a function of temperature using a steep freezing function (Case 1a,b) and a smooth (low slope) freezing function (Case 2a,b). See Equation 5 and Table 2 for parameter definitions.

75x98mm (220 x 220 DPI)

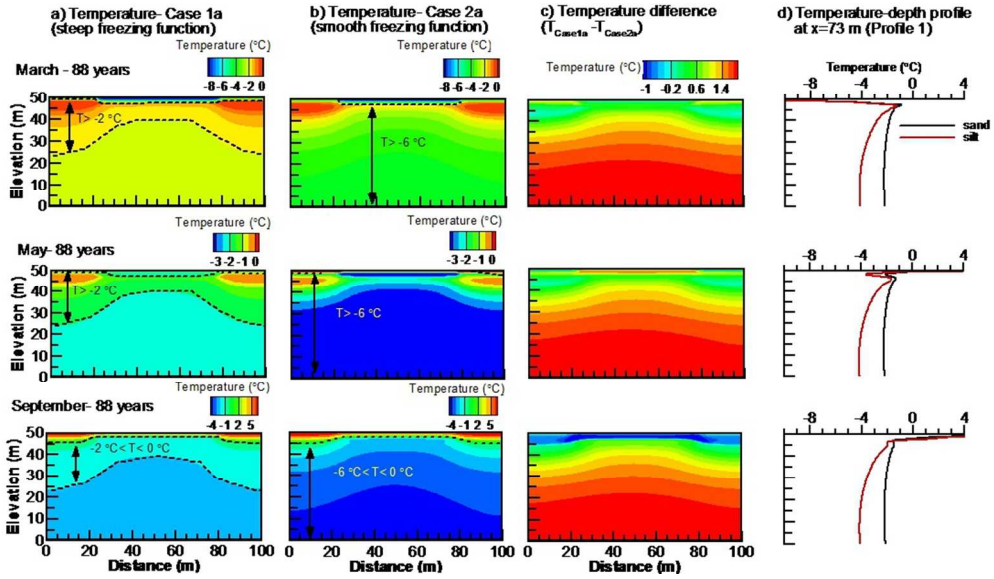

Figure 5. Simulated temperature distributions for a) Case 1a (homogeneous system, steep freezing function) and b) Case 2a (homogeneous system with a smooth freezing function), for March, May and September after 88 years; conductive heat transport only. The temperature difference between these two cases, and the corresponding vertical profiles (at x=73 m), are shown in (c) and (d), respectively. The vertical arrows identify the phase-change regions where water and ice co-exist.

231x133mm (120 x 120 DPI)

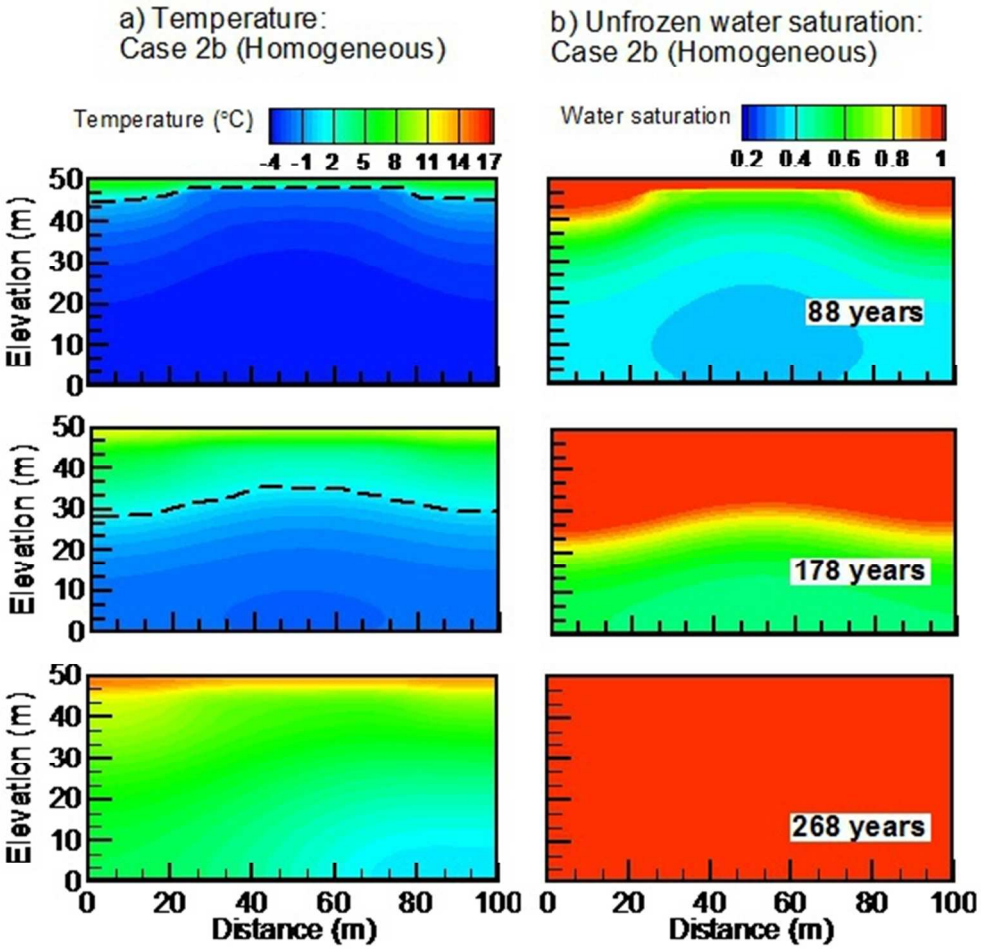

Figure 6. Thermal behaviour resulting from advective-conductive heat transport in the homogeneous system, with a smooth freezing function, under climate warming, showing a) ground temperatures, and b) the respective corresponding evolution of unfrozen water saturation. The simulation results are plotted for the month of September after the 88th, 178th, and 268th year. The dashed lines show the location of the thaw front (0 °C).

121x121mm (120 x 120 DPI)

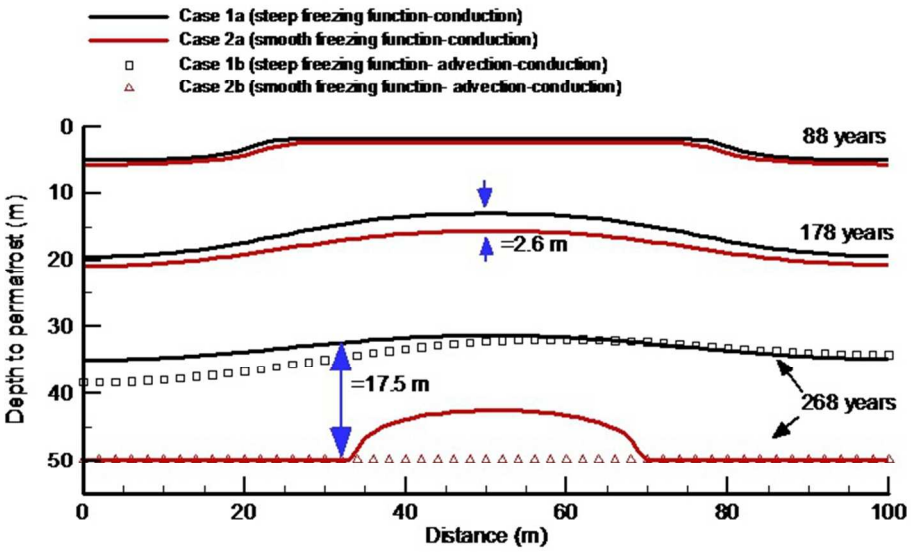

Figure 7. Simulated spatial and temporal locations of the depth to permafrost (thaw front below the active layer) using different freezing functions in a homogeneous system, for cases with a steep freezing function (Case 1a,b) compared to a gentle function (Case 2a,b), over 268 years under conductive (solid line) and advective-conductive (symbols) heat transport. The blue arrows show the maximum difference in depth to permafrost between the two conduction-only cases after 178 and 268 years.

164x93mm (120 x 120 DPI)

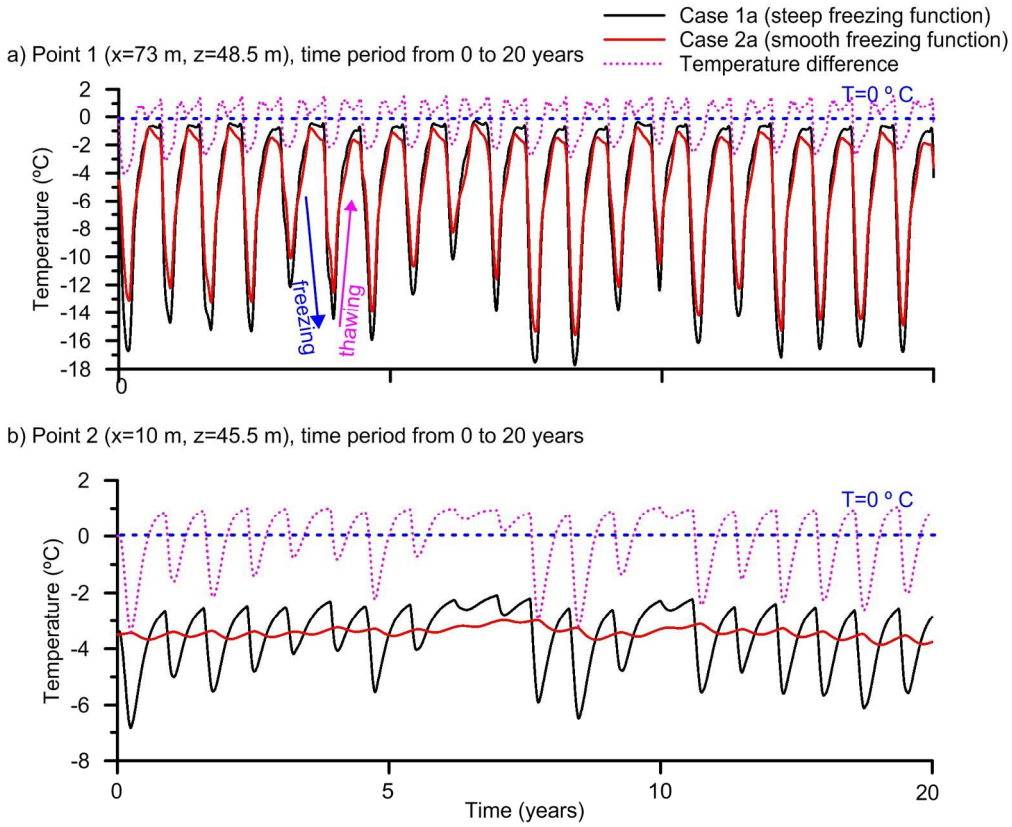

Figure 8. Temperature changes over time (0-20 years) at monitoring points 1 and 2 ((a) and (b), respectively; see locations in Figure 2), using a steep freezing function and smooth freezing function as shown in Figure 4 and defined in Table 2. Point 1 is about 1.5 m below the right embankment (at 48.5 m elevation) and Point 2 is about 4.5 m below the left embankment (at 45.5 m elevation). The temperature differences between the two soil cases, at each monitor point, are shown as a dashed pink line.

166x136mm (299 x 299 DPI)

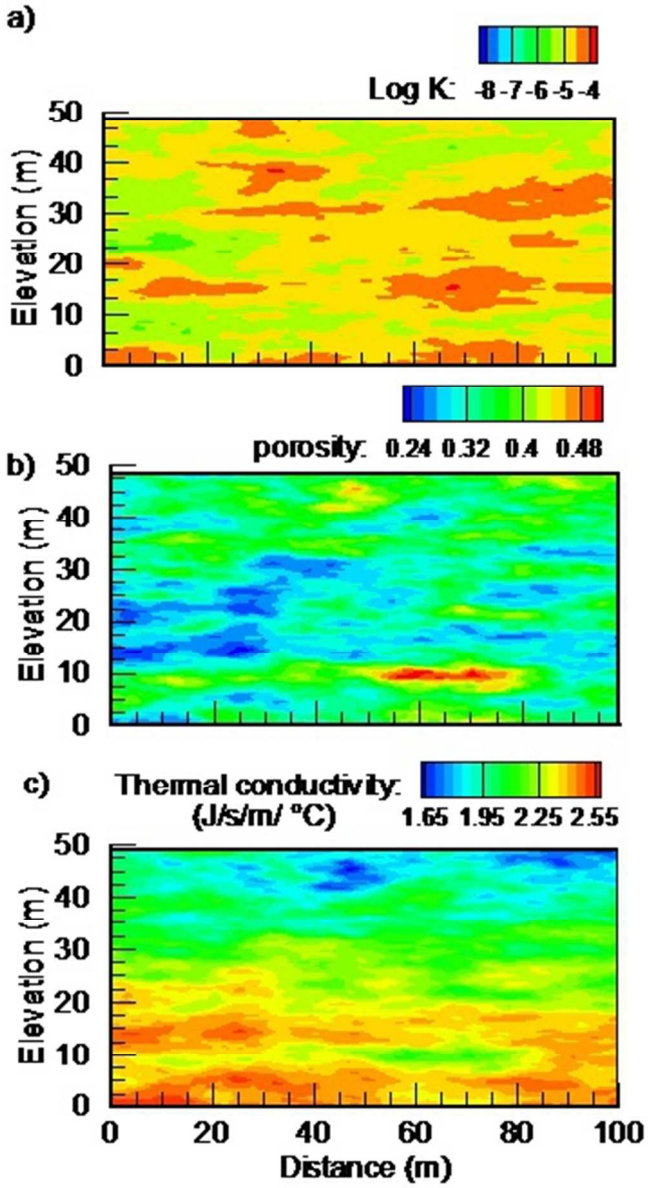

Figure 9. Heterogeneous Cases 3a,b: a) initial stochastic *K* field (log K m s^{-1}), b) the inversely-correlated porosity distribution, and c) the initial thermal conductivity distribution. See Table 1 for stochastic parameters.

84x140mm (120 x 120 DPI)

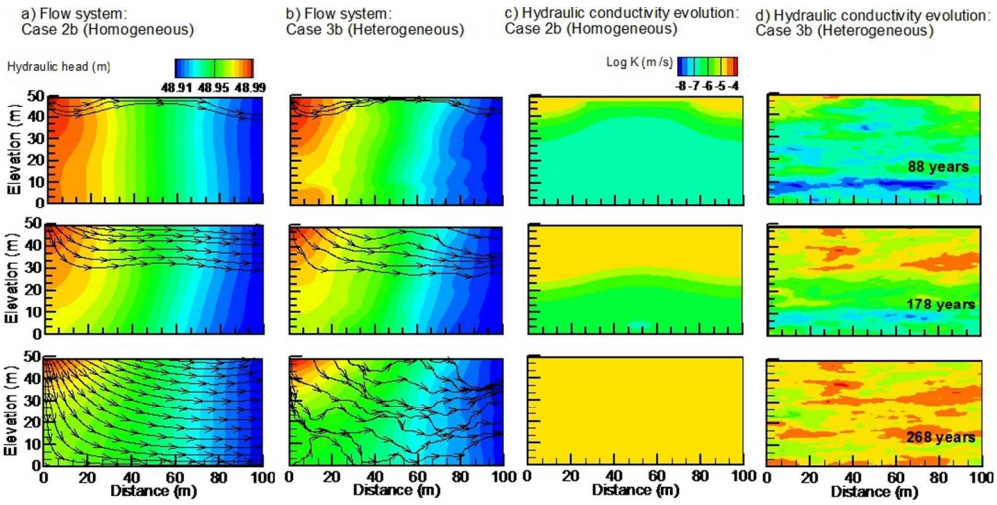

Figure 10. Temporal and spatial evolution of the simulated flow systems (equipotentials and flow paths), resulting from a) a homogeneous soil and b) a heterogeneous system, and c-d) the respective evolution of hydraulic conductivity, under the future climate scenario for Cases 2b and 3b, respectively.

230x114mm (120 x 120 DPI)

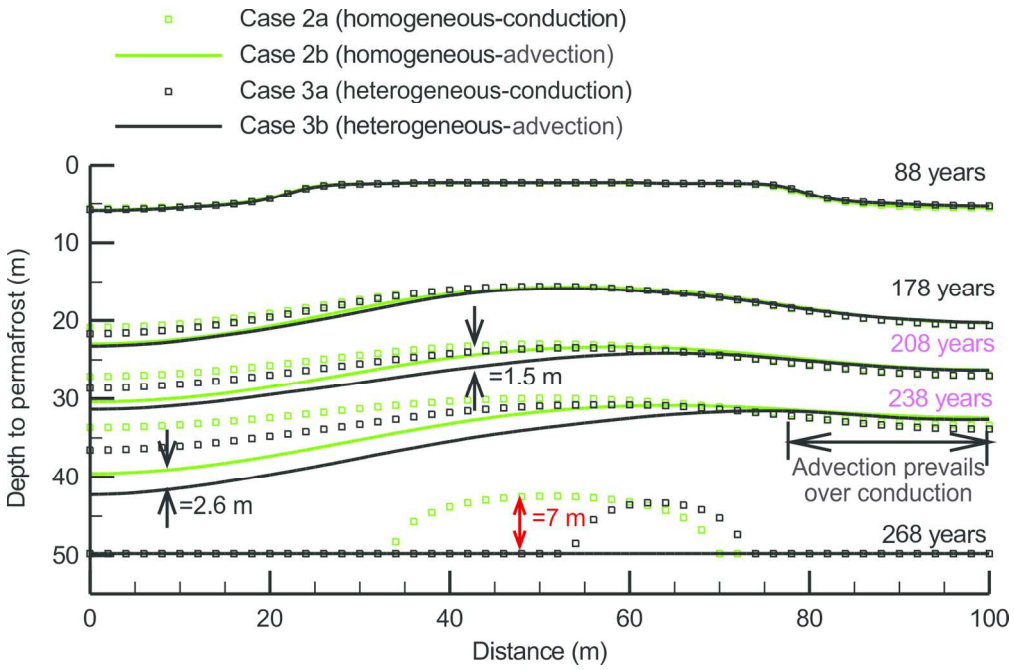

Figure 11. Simulated spatial and temporal distribution of the depth to permafrost comparing the completely homogeneous soil (Case 2a,b) to a heterogeneous soil with a stochastic K and porosity field (Case 3a,b), under conduction-only and advective-conductive driven thaw, based on the climate scenario over 88, 178, 208, 238 and 268 years. Vertical black arrows identify the maximum differences in depth to permafrost between the homogeneous and heterogeneous cases under advection-conduction while the red arrow identifies the corresponding maximum difference under conduction alone after 268 years.

148x97mm (300 x 300 DPI)